Vertical Distribution of Heat and Sodium Fluxes in the Mesopause Region Measured by Sodium Lidar Over Hainan, China (109°E,19°N)

Xingjin Wang[1,2,3], Xin Fang[1,2,3*], Wenhao Gao[1,3,†], Xianhang Chen[1,3],Tai Liu[4],
Chengyun Yang[1,3], Tingdi Chen[1,2,3], Tao Li[1,3], Xianghui Xue[1,2,3]

[1] National Key Laboratory of Deep Space Exploration/School of Earth and Space Sciences, University of Science and Technology of China, Hefei, Anhui, China.

[2]Hefei National Laboratory, University of Science and Technology of China, Hefei, China.

[3] CAS Center for Excellence in Comparative Planetology/CAS Key Laboratory of Geospace Environment/Mengcheng National Geophysical Observatory, University of Science and Technology of China, Hefei, Anhui, China.

[4]Department of Geophysics, College of the Geology Engineering and Geomatics, Chang'an University, Xi'an, 710054, China.

[†]deceased, 9 September 2024.

*Correspondence to: Xin Fang (xinf@ustc.edu.cn)

Abstract. We present the first lidar-based characterization of seasonal variations in gravity–wave induced vertical heat flux, sodium flux, and associated parameters—sodium density and temperature—between 80 and 100 km over Hainan, China (19° N, 109° E). Observations were carried out using a narrow band sodium lidar equipped with a laser frequency-locking and real-time monitoring module, achieving a root-mean-square (RMS) frequency stability of 0.5 MHz. Since February 2024, the system has provided continuous measurements of mesospheric sodium density, temperature, and vertical wind. The lidar results are generally consistent with coincident satellite measurements and model simulations at the near geographic location. Observations indicate that the highest temperatures below 95 km occur in May and November, with seasonal patterns closely matching from the SABER satellite data. The annual mean vertical heat flux shows two peak descent rates, -1.21 K m s^{-1} at 89 km and -1.38 K m s^{-1} at 92 km, corresponding to a cooling rate of approximately 95 K day^{-1} between 82 and 97 km. The sodium flux reveals pronounced maxima exceeding -65 m s^{-1} cm^{-3} at 92, with the resulting dynamical transport producing a maximum net sodium loss of 75 cm^{-3} h^{-1} near 93 km.

1. Introduction

In the mesopause region, ranging from approximately 80 to 100 km in altitude, temperature and wind are critical atmospheric parameters for understanding the dynamics of this region. Measurements of atmospheric parameters in this region enable investigations of dynamic and photochemical processes in the upper mesosphere, which also serves as a transition zone of importance to aviation and aerospace activities (Li et al., 2018; Sheng et al., 2025). Since the 1970s, ground-based instruments and spaceborne sensors have been extensively employed to measure key parameters (Cox et al., 1993; Gardner et al., 1986; She et al., 1998; Vincent and Reid, 1983; Wu et al., 2008). Compared to the satellites and medium-frequency radars, narrow band sodium lidars offer the unique capability to simultaneously measure temperature and horizontal wind in the mesopause region by leveraging the high-resolution sodium emission spectrum (Arnold and She, 2003; She and Yu, 1994; Vincent and Reid, 1983).

Heat and compositional variations in the mesopause range are primarily driven by atmospheric gravity waves (AGWs) through their influence on global circulation. AGW-driven vertical transport of heat and constituents is expressed by the vertical fluxes of sensible heat and species densities, defined as the expected values of the product of vertical wind fluctuations (w′) and the corresponding fluctuations in temperature (T′) or constituent density (ρ'_{Na}), induced by the gravity wave spectrum (Chu et al., 2022; Gardner, 2024; Liu and Gardner, 2005). Measurements from the Sodium Resonance Lidar at the Starfire Optical Range (SOR) in New Mexico show that the maximum downward dynamical flux of sodium (Na) can reach -280 m·s^{-1}·cm^{-3} at ~88 km, indicating that dynamical transport often exceeds the vertical transport associated with eddy diffusion (Liu and Gardner, 2004). In contrast to the short-period (<1 h) waves reported to drive heat transport elsewhere (Guo and Liu, 2021), observations at Hefei indicate that long-period gravity waves (>1 h) dominate the mesopause heat flux (Li et al., 2022).

In this study, we report on a newly developed narrowband high-spectral-resolution sodium lidar system, designed by the University of Science and Technology of China (USTC). This system builds upon the earlier USTC narrowband sodium temperature and wind lidar based on a self-developed pulsed dye amplifier (PDA). Specifically, the new 589 nm lidar employs a more stable and powerful single-frequency Raman fiber amplifier, along with new designs that integrate an enhanced timing control system and a more precise frequency locking unit based on modulation transfer spectroscopy (MTS)

technology. Furthermore, beat frequency technology is used to monitor frequency jitter of between pulsed and continuous-wave laser in real time.

From February 2024 to January 2025, routine measurements of sodium density, temperature, and vertical wind were obtained to calculate sensible heat flux and sodium flux over Hainan, China. Section 2 provides a detailed description of the lidar system and its technical improvements. Section 3 presents monthly averaged results of sodium density and temperature, including comparisons with SABER satellite and the MSISE model data, thereby confirming the reliability of the lidar data for scientific research. At the same time, the amplitudes of harmonic fitting for the annual, semi-annual, 4-month and 3-month periods in Hainan region are given. Section 4 discusses the annual average sensible heat flux associated with AGWs and its seasonal profiles, as well as its influence on the heating and cooling effects of the background atmosphere over Hainan. In addition, the annual average and seasonal variations of sodium flux were provided, including the corresponding sodium production rate. Section 5 summarizes the main conclusions.

2. Lidar System Setup

In this section, we present an overview of the technical enhancements implemented in the lidar system. A schematic diagram of the narrow band sodium lidar deployed in Hainan is shown in Fig. 1, a photograph of the system in Fig. 2, and the corresponding system parameters are summarized in Table 1.

The lidar system consists of three main components: a transmitter, a receiver, and a signal detection and control module. The lidar transmitter system includes three commercial lasers (Semiconductor seed laser, Raman amplified laser, 1064 nm seed laser and Nd: YAG laser), a self-made pulsed dye amplifier (PDA), and a set of custom-engineered module for absolute frequency locking with self-calibration. A semiconductor seed laser (DL Pro) emits 1178 nm continuous-wave laser with a maximum power of 70 mW. The 1178nm seed laser after pre-amplification is split into two beams. One beam is frequency-doubled using a Periodically Poled Lithium Niobate (PPLN) crystal for frequency locking, while the other beam is frequency-shifted by three frequencies using a fiber acousto-optic frequency shifter (AOFS) module and then undergoes secondary amplification to obtain a three-frequency 589nm laser, with the average power of approximately 1.5 W.

3

85　　A Nd: YAG laser (Continuum PLS 9050e) produces 532 nm pulses at 50 Hz with a maximum energy of 600 mJ and a pulse duration of 9 ns. The amplified three-frequency 589 nm laser is further amplified and pulsed through a three-stage traveling-wave amplification system by the 532 nm pulsed laser at 400 mJ and the 589 nm continuous-wave laser at 1.5 W, yield a three-frequency 589 nm pulsed laser with 30 mJ energy, 6 ns pulse width, and a beam diameter of 7 mm.

90　　The backscattered photons after the interaction of the 589 nm pulsed laser with sodium atoms in the atmosphere are collected by a telescope with a diameter of 1 m and 1.7 m focal length. The photons then pass through a collimating lens, a narrow band optical filter, and a converging lens before being focused onto the active area of a photomultiplier tube (PMT). A high-speed photon counter records the photons counts, from which vertical profiles of sodium atomic density, temperature, and vertical wind velocity in
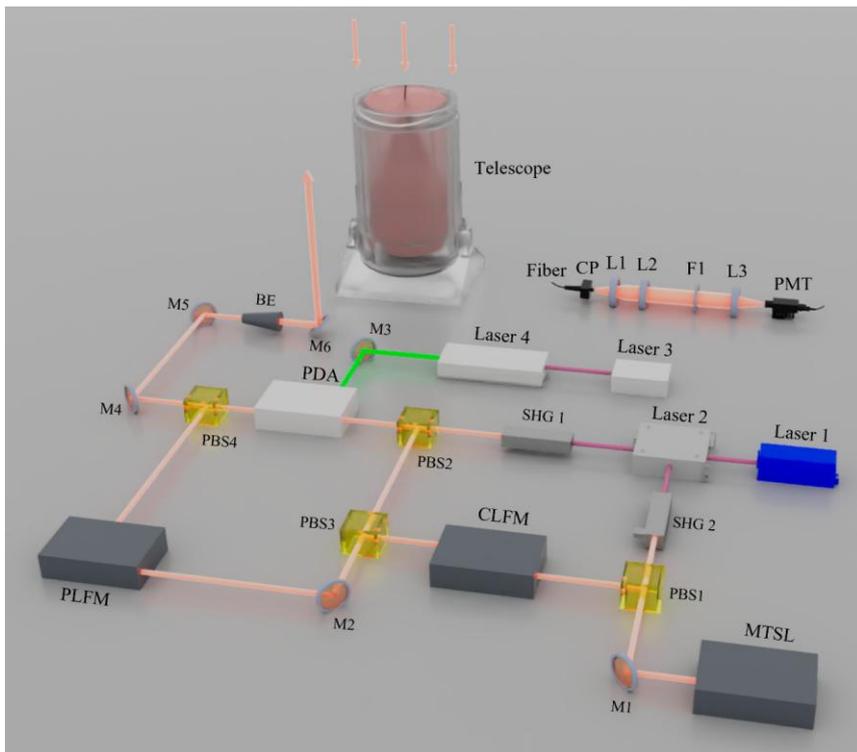
95　　the sodium layer are derived.

Figure 1. Schematic diagram of the lidar system. Laser 1, semiconductor seed laser; Laser 2, Raman amplified laser; Laser 3, 1064 nm seed laser; Laser 4, Nd: YAG laser; SHG, second-harmonic generation; PBS, polarizing beam splitter; M, mirror; BE, beam expander; CP, Chopper; L, lens; F, filters; PMT, photo

100

Figure 2. Photo of the lidar system.

Table 1. Lidar Parameters

Transmitter	Wavelength	589.158 nm
	CW seeder laser into PDA	＞0.5 W
	Nd: YAG laser	20 W
	Linewidth	~120 MHz
	Pulse energy of 589 nm	~30mJ
	Repetition rate	50 Hz
	Pulse width	6 ns
	Beam divergence	0.7 mrad
Receiver	Telescope aperture	1 m
	Field of view	0.88 mrad
	Bandwidth of filter	1 nm
	Bin width	61.44 m

105   The main technical improvements of this lidar system. Fig. 3a illustrates the schematic of the laser emission system. The absolute frequency locking and monitoring module of the laser is shown in detail, comprising a modulation transfer spectroscopy (MTS) unit, a continuous-wave 589nm frequency

5

monitoring unit based on iodine absorption, and a laser frequency jitter monitoring unit between the continuous-wave and pulsed 589nm laser.

2.1 Modulation Transfer Spectroscopy (MTS) Locking unit

The modulation transfer spectroscopy (MTS) method involves applying a modulation signal to an electro-optic modulator (EOM), which generates sidebands that beat with the carrier frequency. A photodetector is then used to detect and demodulate the resulting heterodyne signal, allowing atomic modulation transfer spectral lines to be resolved.

To eliminate Doppler broadening, a pair of counter-propagating laser beams is implemented. As illustrated in Fig. 3c, the high-power pump beam is modulated by an EOM, while the low-power beam serves as the probe beam. The two beams are spatially overlapped and propagate in opposite directions. When the laser frequency approaches the atomic transition, sidebands are generated on the probe beam via the four-wave mixing effect, transferring the modulation from the pump beam to the probe beam. A photodiode (PD1) detects the probe beam, and demodulation of the signal yields the frequency stabilization error signal.
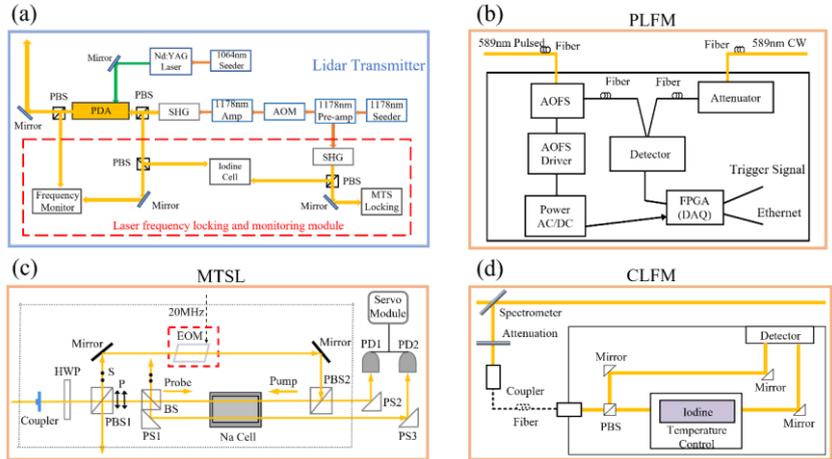

Figure 3. Schematic diagram of (a) the lidar transmitter, (b) pulsed laser frequency monitoring (PLFM) unit, (c) modulation transfer spectroscopy locking (MTSL) unit, (d) continuous laser frequency monitoring (CLFM) unit of the lidar system.

2.2 Continuous Laser Frequency Monitoring unit

Because the single-frequency Raman amplifier generates two laser beams, the MTS was used to lock the frequency of one low-power beam to the sodium D_{2a} line. Simultaneously, the frequency difference between the second beam and the locked beam is tracked in real time. The iodine molecular transmission spectrum near the sodium D_{2a} line is employed to calibrate the relationship between laser frequency and iodine cell transmittance, enabling frequency-difference tracking. Once the laser frequency is locked, the iodine transmittance is monitored in real time to evaluate frequency stability and locking accuracy. The optical configuration is shown in Fig. 3d.

Figure 4 presents the results of laser frequency monitoring. In the unlocked state, the laser frequency drifts freely with an amplitude of ~20 MHz over 22 minutes. After applying MTS-based frequency locking, the frequency jitter is reduced to within ±1 MHz of the designated output frequency.
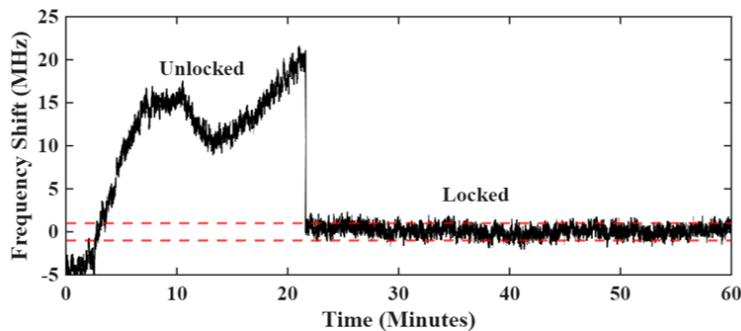

Figure 4. Continuous laser frequency monitoring results.

2.3 Pulsed Laser Frequency Monitoring unit

Since the detected signal originates from pulsed laser with a 50 Hz repetition rate, it is essential to measure the frequency shift induced by the chirp effect of the PDA. To achieve this, three acousto-optic frequency shifters (AOFS) are used to shift the frequency of the frequency-locked 589 nm continuous-wave beam by 1150 MHz. The pulsed laser emerging from the PDA is then mixed with the shifted continuous-wave laser to generate a heterodyne signal. This signal is detected and demodulated to determine the real-time frequency shift. Subtracting the known 1150 MHz offset yields the actual frequency difference between the pulsed and continuous beams. The optical configuration is illustrated in Fig. 3b.

7

As shown in Fig. 5b, the frequency difference between the 589 nm continuous-wave and pulsed beams measured on 7 July 2024, was approximately -14.9 MHz, corresponding to a vertical wind offset of -8.77 m s^{-1}. The monitoring results (Fig. 5a) indicate a frequency stability of ±1 MHz, its root mean square (RMS) is almost 0.5MHz. The average vertical wind velocity throughout the night is approximately -9 m s^{-1}, consistent with the offset determined from frequency monitoring unit.
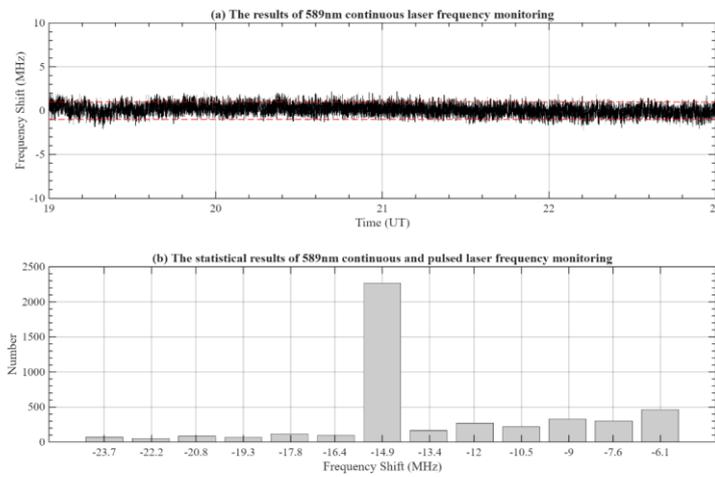

Figure 5. Results of the laser frequency locking and monitoring module on 7 July 2024. (a) the results from continuous laser frequency monitoring unit; (b) the statistical results from continuous and pulsed laser frequency monitoring unit.

A comparison in Fig. 6 reveals consistent trends between the nightly-mean-subtracted vertical wind (black dashed line) and the frequency-offset-corrected wind (blue solid line), with the latter resolving finer atmospheric structures. This agreement demonstrates the capability of the frequency monitoring module to effectively correct systematic instrumental biases.
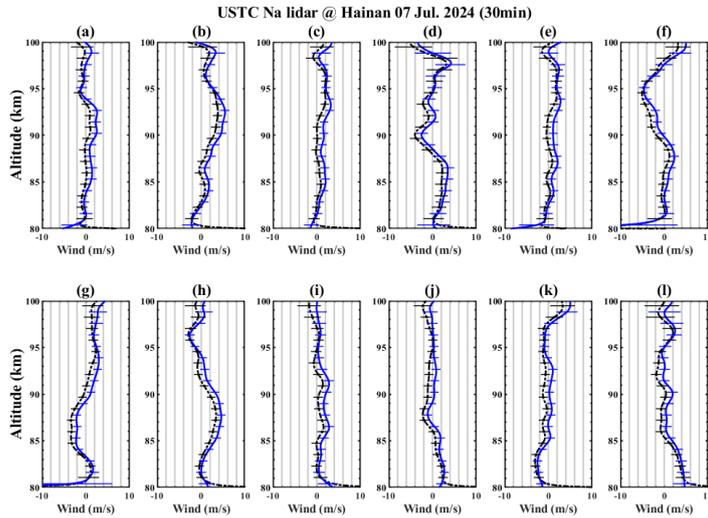
USTC Na lidar @ Hainan 07 Jul. 2024 (30min)

Figure 6. Sodium layer vertical wind (black dashed line) and the vertical wind after correcting frequency offset (blue solid line) at 30 minutes on 7 July 2024. Error bars are shown as thin lines.

2.4 Summary of Section 2:

The integration of absolute frequency locking and real-time self-calibration allows accurate measurement of the frequency difference between the pulsed 589 nm laser and the sodium D_{2a} spectral line. These capabilities ensure precise vertical wind retrievals, validating the stability and performance of the Hainan sodium lidar.

3. Na Lidar Initial Results and Processing

3.1 Initial Results

The raw signals were recorded as photon counts with a vertical resolution of 61.44 m and a temporal resolution of 1 minute (corresponding to 3000 laser pulses). Sodium density, temperature, and vertical wind were calculated by integrating the photon counts over 30 minutes, with a vertical resolution of 2 km (Wang et al., 2025).

In this section, we compare sodium layer temperatures measured by the lidar system with those from SABER satellite observations and the MSISE model across different seasons (Fig. 7). More wave-like structures in the SABER and lidar temperature profiles are likely attributable to gravity waves, since

SABER requires only ~1.5 min to produce a single profile. Although measurement locations may differ

180   by several hundred kilometers, the temperature profile trends among the three datasets are broadly

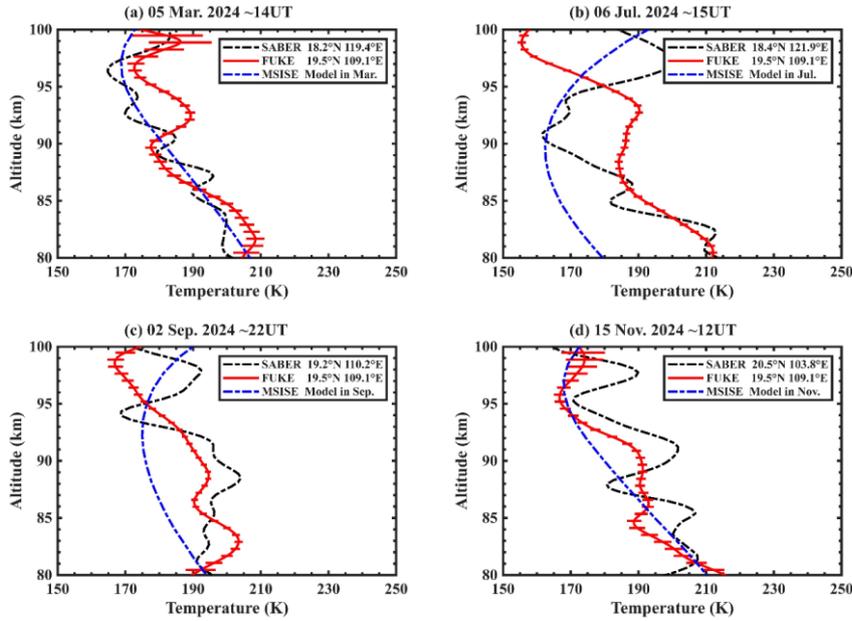consistent, confirming the reliability of the lidar observations.

Figure 7. Typical profiles of temperature measured by lidar (red solid line), SABER (black dashed line) and MSISE (blue dashed line) in different seasons. (a) spring, (b) summer, (c) autumn, (d) winter. Error bars are
185   **shown as thin lines.**

3.2 Seasonal Variations in Sodium Density and Temperature

To investigate seasonal variations in sodium density and temperature over Hainan, 53 observational

samples were selected between February 2024 and January 2025, with a cumulative duration exceeding

326 hours. Figure 8 shows the monthly distribution of the number of nights with valid lidar data, along
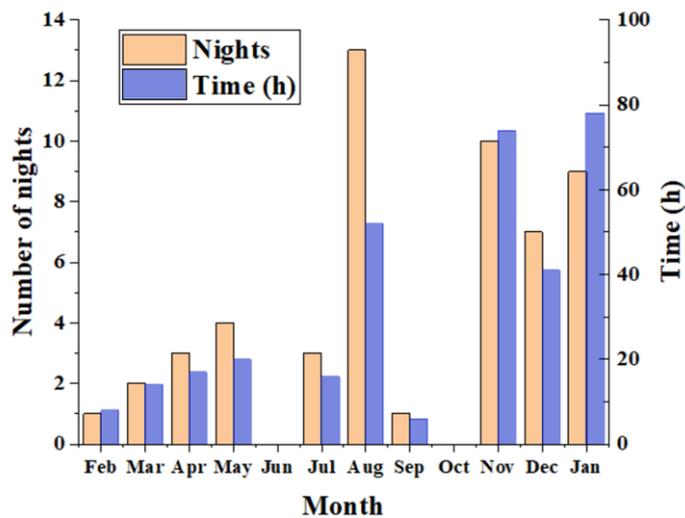
190   with the corresponding observation times.

Figure 8. Histogram of number of nights and hours with valid data observed by the USTC sodium lidar at Hainan.

As illustrated in Fig. 9, the monthly-averaged sodium number density exhibits a peak altitude range between ~85 and 96 km, centered near 91 km. The centroid height varies seasonally: ~93-95 km in spring, decreasing to ~90 km in late summer and autumn (beginning in August). In winter (around November), the peak density reaches its annual maximum of over 4200 cm^{-3} at 91 km, whereas from February to September, the peak remains in the range of 3000-3500 cm^{-3}.

Overall, seasonal variability in sodium density over Hainan is pronounced, with monthly averages generally above 3000 cm^{-3}. When combined with the monthly-mean temperatures shown in Fig. 10, the relationship between sodium density and temperature is consistent with previous findings from the Hefei narrow band sodium lidar: below 95 km, sodium density correlates positively with temperature, suggesting strong chemical control on sodium production; above 95 km, sodium density exhibits a negative correlation with temperature (Li et al., 2018).

11
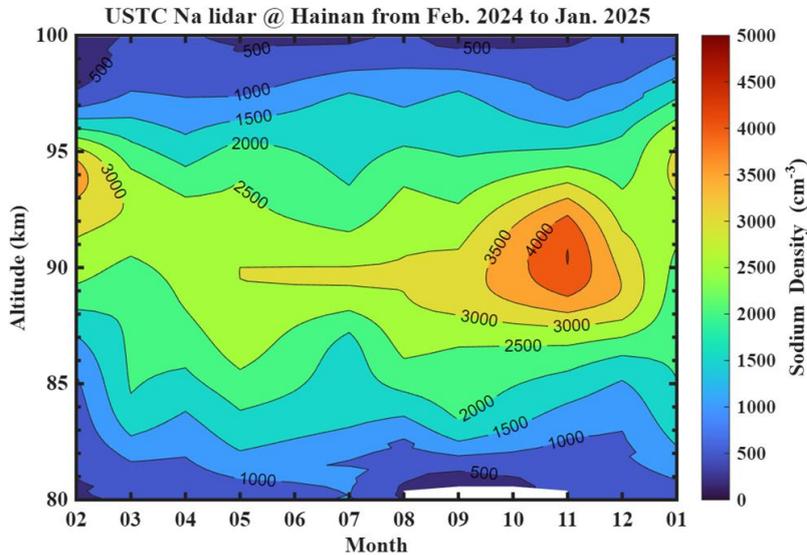
USTC Na lidar @ Hainan from Feb. 2024 to Jan. 2025

Figure 9. Monthly mean of nightly sodium density observed by lidar.

Figure 10 compares monthly mean temperatures derived from the Hainan sodium lidar with those from the SABER satellite. For the SABER dataset within ±5° latitude/longitude of the lidar site were selected, and only data coinciding with the lidar observation periods were included. These were averaged monthly to represent the temperature distribution.

The vertical temperature structure observed over Hainan (19° N, 109° E) differs slightly from that at Hefei (32° N, 117° E), although monthly means are comparable. Below 95 km, temperatures range from ~185 K to 210 K, while above 95 km they decrease to ~170-185 K (Li et al., 2018).

The seasonal trends of lidar and SABER temperatures over Hainan are generally consistent, though small discrepancies in absolute values remain. Below 95 km, lidar observations report higher autumn–winter temperatures compared with SABER and mid-latitude Hefei measurements. This is likely linked to meridional circulation at the mesopause, with upward motion in the summer hemisphere and downward motion in the winter hemisphere. Above 95 km, lidar temperatures are ~5-10 K lower than SABER, likely due to either the reduced signal-to-noise ratio at higher altitudes in lidar retrievals (Li et al., 2012) or non-local thermodynamic equilibrium (non-LTE) effects in SABER retrievals (Mertens et al., 2001).
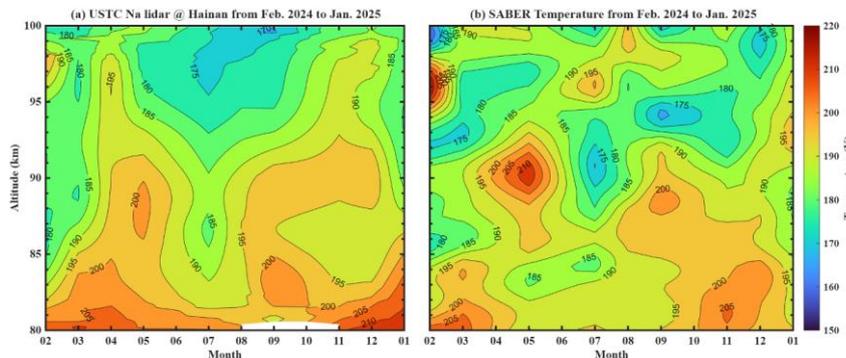
Figure 10. Monthly mean of nightly mean temperature observed by (a) lidar and (b) SABER.

Figure 11 presents the amplitudes of the annual, semi-annual, 4-month, and 3-month harmonic fits for the Hainan region. Due to the one-year dataset with observations primarily confined to winter, the fitting uncertainty increases for shorter periods; thus, we only consider the annual and semi-annual components robust. For context, Table 2 compares the seasonal temperature variations at several sites in both hemispheres. The observed maximum amplitude of ~7 K at 85 km is closer to the 9.5 K value reported from Maui than to those of high-latitude stations, suggesting a potential signature of low-latitude mesopause dynamics (Chu et al., 2005).
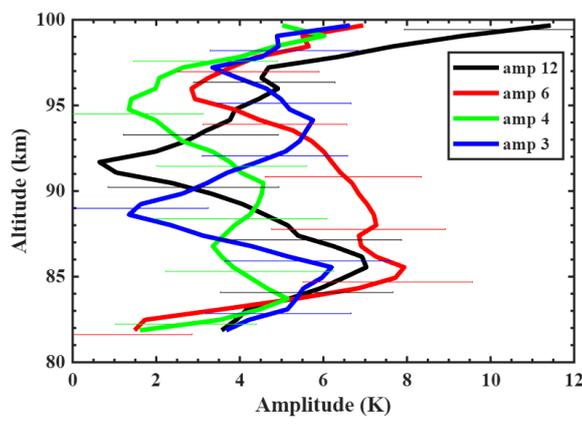
Figure 11. Seasonal harmonic amplitude profiles with the period of 12 (black), 6 (red), 4 (green), and 3 (blue) months. Error bars are shown as thin lines.

Table 2. Summary of Annual (12 months) Temperature Variations in the Mesopause Region

		Low-altitude maximum		High- altitude minimum	
Site	References	Altitude	12-month	Altitude	12-month

13

			amplitude		amplitude
S Pole (90°S)	(Pan and Gardner, 2003)	85 km	32K	99 km	3.0K
Syowa (69°S)	(Kawahara et al., 2004)	84 km	30K	98 km	5.0K
Kühlungsborn (54°N)	(Gerding et al., 2008)	85 km	28K	102 km	3.0K
CSU (40.6°N)	(She et al., 2022)	85.5 km	20K	98 km	1.0K
Urbana (40°N)	(States and Gardner, 2000)	85 km	14K	97.5 km	1.0K
Starfire (35°N)	(Chu et al., 2005)	87 km	15K	96.5 km	1.0K
Maui (20.7°N)	(Chu et al., 2005)	86 km	9.5K	97 km	3.5K
Hainan (19.5°N)	This manuscript	85.5 km	7K	92 km	0.7K

4. Gravity Wave Vertical Flux

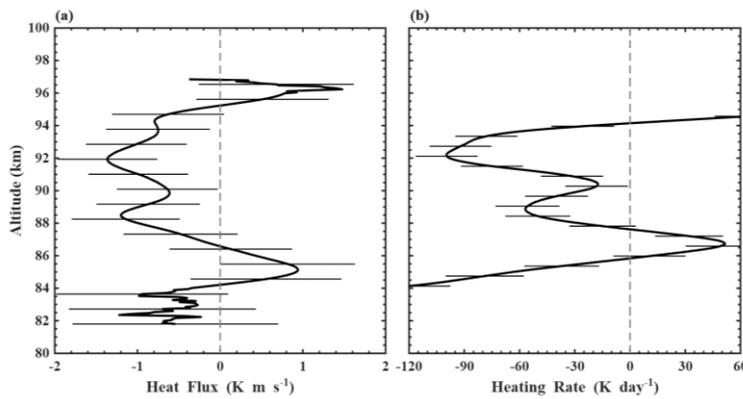### 4.1 Heat Flux

The vertical fluxes of sensible heat (w′ T′) and sodium density (w′ ρ'_{Na}) were calculated using data with vertical and temporal resolutions of Δz = 2 km and Δt = 3 minutes, respectively. The heat flux over Hainan is shown in Fig. 12a and is predominantly downward, consistent with theoretical expectations (Walterscheid, 1981; Weinstock, 1983). Two distinct downward flux peaks are observed: -1.21 K·m s^{-1} at 89 km and -1.38 K·m s^{-1} at 92 km. By contrast, at Hefei, a single peak of -2 K·m s^{-1} typically occurs around 88 km except in summer (Li et al., 2022). This difference suggests that the altitude and magnitude of gravity wave dissipation vary across locations.

The corresponding heating rates (Fig. 12b), derived from the divergence of the dynamical heat flux, show a maximum cooling rate exceeding 95 K day^{-1} at 92 km—a value comparable to radiative contributions. These results highlight the critical role of gravity wave dissipation in maintaining the thermal balance of the mesopause region (Liu and Gardner, 2005).

At the Starfire Optical Range (SOR, 35° N), seasonal variations in sensible heat flux display a strong semiannual pattern, with maximum downward fluxes of -2 to -3 K·m s^{-1} near 88 km during early November to early February, and minima of ~-0.5 K·m s^{-1} around the equinoxes (Gardner and Liu, 2007).

Measurements at Maui, Hawaii (20.7° N), also reveal notable seasonal features. The annual mean heat flux exhibits a double-peak structure, with two downward maxima of -1.25 K·m s^{-1} at 87 km and -1.4 K·m s^{-1} at 95 km (Liu and Gardner, 2005). This structure is similar to that observed in Hainan, which lies at a comparable latitude but different longitude.

14

More recently, Guo and Liu reported seasonal variations in vertical GW heat flux over Cerro Pachón, Chile (30° S). Their results showed strong annual and weaker semi-annual oscillations, with maximum downward fluxes in June–July. The flux profile exhibited a broad maximum extending from 88 to 94 km, with average values around -2.5 K·m s^{-1}, consistent with peak values observed in late May at McMurdo (Guo and Liu, 2021).
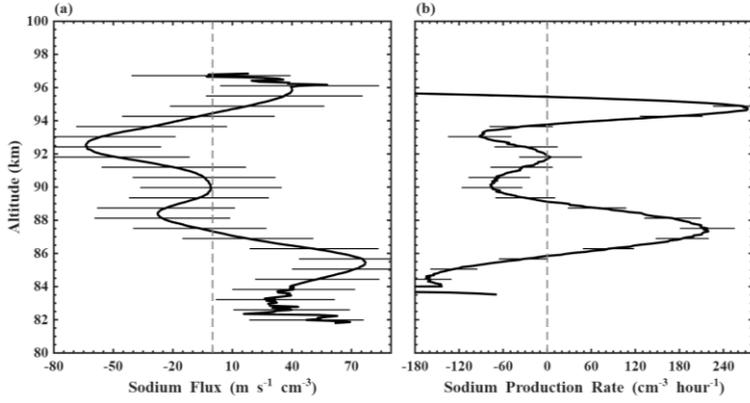

Figure 12. The vertical flux of sensible heat. (a) Annual mean sensible heat flux derived from vertical wind and temperature measurements at Hainan, China, and (b) the corresponding heating rates. Error bars are shown as thin lines.

4.2 Sodium Flux

The dynamical flux of sodium is shown in Fig. 13a. Over Hainan (19.5° N, 109.1° E), the measured sodium flux exhibits peaks exceeding -65 m s^{-1}·cm^{-3} at altitudes of 92 km. This transport results in a net sodium loss peaking near 93 km, with a downward flux rate of ~75 cm^{-3}·h^{-1}. At Maui (20.7° N), the maximum flux is slightly larger (-80 m s^{-1}·cm^{-3}), while at Hefei (32° N, 117° E), values are smaller (-30 m s^{-1}·cm^{-3}) in the 89-95 km altitude range (Chu et al., 2022).

At the Starfire Optical Range (SOR, 35° N), sodium fluxes show strong semiannual variations, with maximum downward values between -175 and -275 m s^{-1}·cm^{-3} near 88 km from early November to early February, and minima around -25 m s^{-1}·cm^{-3} during the equinoxes (Gardner and Liu, 2010). Similarly, observations at Table Mountain, Colorado (40° N), in August–September reported peak values of -150 m s^{-1}·cm^{-3} at 86 km (Huang et al., 2015).

Figure 13. The dynamical flux of sodium. (a) Na flux due to dissipating gravity waves calculated from the measured Na density and vertical wind measurements at Hainan. (b) Na production rate calculated from measured Na flux at Hainan. Error bars are shown as thin lines.

Figure 14a presents the seasonal variation in vertical heat flux. The fluxes in all four seasons generally align with the annual mean, with winter contributing the most, consistent with the observational distribution shown in Figure 8. Notably, a conspicuous ~~negative~~positive anomaly at ~85 km in autumn also corresponds to a feature in the annual average. Similarly, the seasonal sodium flux in Figure 14b shows winter as the dominant contributor. ~~Negative~~Positive anomalies at 86 km in ~~summer~~autumn and 91 km in ~~autumn~~summer are also reflected in the annual mean profile. Compared with winter, the observational data for our spring, summer and autumn seasons are all scarce.
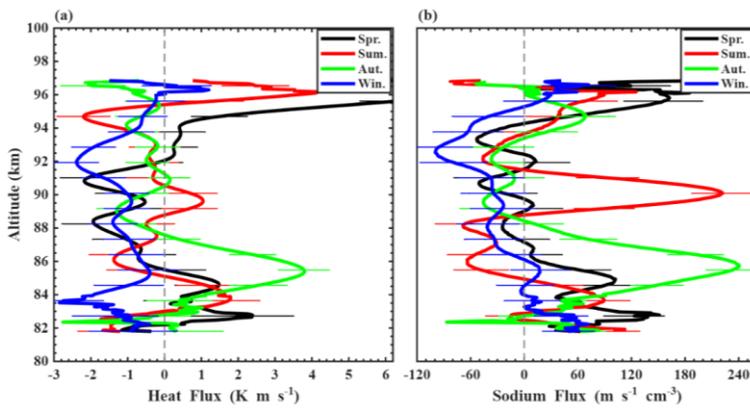
Figure 14. The seasonal profiles of the heat (a) and Na (b) fluxes. Spring (black), summer (red), autumn (green), winter (blue). Error bars are shown as thin lines.

In summary, the heat and sodium fluxes measured at Hainan peak at altitudes similar to those observed at other latitudes and longitudes. However, the absolute magnitudes of sodium fluxes are smaller than at

290 most other sites. A comparison of annual mean gravity wave heat and sodium fluxes across different lidar stations is provided in Table 3.

Table 3. Summary of Heat and Na Fluxes at Different Sodium Lidar Stations

Stations	Table Mountain, Colorado	SOR New Mexico	Hefei, China	Maui, Hawaii	Hainan, China	Cerro Pachón, Chile	McMurdo, Antarctica
~~Latitude and longitude~~References	(Huang et al., 2015)	~~35.0°N 106.5°W~~(Gardner and Liu, 2007; 2010)	~~31.5°N 117.2°E~~(Li et al., 2022; Chu et al., 2022)	~~20.7°N 156.3°W~~(Liu and Gardner, 2005)	~~19.5°N 109.1°E~~This manuscript	~~30.3°S 70.7°W~~(Guo and Liu, 2021)	~~77.84°S, 166.67°E~~(Chu et al., 2022)
Latitude and longitude	40.1°N 105°W	35.0°N 106.5°W	31.5°N 117.2°E	20.7°N 156.3°W	19.5°N 109.1°E	30.3°S 70.7°W	77.84°S, 166.67°E
Observation period	August–September	Late Nov	Fall Mean	Annual Mean	Annual Mean	June	Late May
Resolutions (min)/ (km)	10/0.96	1.5/0.5	10/~3	1.5/0.96	3/~2	1/2	2.5/0.96
Heat flux peak (K m s^{-1})	/	-1.1	-1.04	-1.0	-1.4	-0.4	-3
Heat flux peak altitude (km)	/	~88	89-93	87-95	88-92	~88	~84
Na flux peak (m s^{-1}·cm^{-3})	-150	-225	-30	-80	-65	/	-550
Na flux peak altitude (km)	86	88	89-95	88	92-93	/	~84

格式化表格

5. Summary

The Hainan narrow band sodium lidar, deployed in January 2024 at Hainan, China (19.5° N, 109.1° E),

295 incorporates multiple technical improvements that enable automated operation and enhance usability. A laser frequency-locking and monitoring module continuously tracks the frequency offset between the transmitted laser and the sodium D_{2a} transition, and its stability is verified through vertical wind retrievals

with a frequency jitter below 1 MHz. This capability significantly improves the accuracy of vertical wind measurements.

300 Temperature data from the SABER satellite and the MSISE model were used to validate the scientific reliability of the lidar-based temperature retrievals. Monthly variations of sodium density and temperature in the low-latitude region of Hainan were presented. Comparisons with satellite and model data demonstrated generally consistent patterns, with minor discrepancies comparable to those observed at the mid-latitude Hefei site. The observed maximum amplitude of ~7 K at 85 km is closer to the 9.5 K

305 value reported from Maui than to those of high-latitude stations, suggesting a potential signature of low-latitude mesopause dynamics.

The annual mean heat flux over Hainan exhibits two downward maxima: -1.21 $K \cdot m\ s^{-1}$ at 89 km and -1.38 $K \cdot m\ s^{-1}$ at 92 km. Heat flux divergence indicates a net negative heating rate in the mesopause region, contributing approximately -95 $K\ day^{-1}$ to the background atmosphere between 82 and 97 km. Sodium

310 fluxes display pronounced peaks exceeding -65 $m\ s^{-1} \cdot cm^{-3}$ at 92 km, with the resulting transport producing a maximum sodium loss rate of 75 $cm^{-3} \cdot h^{-1}$ near 93 km. This study therefore provides the first report of seasonal variations in gravity-wave–induced vertical fluxes over Hainan.

Direct measurement of heat flux associated with gravity wave dissipation remains challenging, since the signals are weak relative to the large instantaneous variability of wind and temperature. Substantial

315 temporal averaging is thus required to reduce uncertainties. The present results are derived from more than 300 hours of observations. Continued long-term measurements of wind and temperature with the Hainan sodium lidar will further improve the precision of flux estimates and deepen understanding of gravity-wave–driven processes in the mesopause region.

contributed to the scientific discussion. TC, XC and TL provided support for the data curation. TC contributed to the project administration. XF and XX acquired the research funding. All co-authors contributed to proofreading of the manuscript.

References

Arnold, K. S., & She, C.: Metal fluorescence lidar (light detection and ranging) and the middle atmosphere. Contemp. Phys., 44(1), 35-49.https://doi.org/10.1080/00107510302713, 2003.

Chu, X., Gardner, C. S., & Franke, S. J.: Nocturnal thermal structure of the mesosphere and lower thermosphere region at Maui, Hawaii (20.7 N), and Starfire Optical Range, New Mexico (35 N). J. Geophys. Res.-Atmos., 110(D9). https://doi.org/10.1029/2004JD004891, 2005.

Chu, X., Gardner, C. S., Li, X., & Lin, C. Y. T.: Vertical transport of sensible heat and meteoric Na by the complete temporal spectrum of gravity waves in the MLT above McMurdo (77.84 S, 166.67 E), Antarctica. J. Geophys. Res.-Atmos., 127(16), e2021JD035728. https://doi.org/10.1029/2021JD035728, 2022.

Cox, R., Plane, J., & Green, J.: A modelling investigation of sudden sodium layers. Geophys. Res. Lett., 20(24), 2841-2844. https://doi.org/10.1029/93GL03002, 1993.

Gardner, C. S., Voelz, D., Philbrick, C., & Sipler, D.: Simultaneous lidar measurements of the sodium layer at the Air Force Geophysics Laboratory and the University of Illinois. J. Geophys. Res.-Space

Phys., 91(A11), 12131-12136. https://doi.org/10.1029/JA091iA11p12131, 1986.

Gardner, C. S., & Liu, A. Z.: Seasonal variations of the vertical fluxes of heat and horizontal momentum in the mesopause region at Starfire Optical Range, New Mexico. J. Geophys. Res.-Atmos., 112(D9). https://doi.org/10.1029/2005JD006179, 2007.

360   Gardner, C. S., & Liu, A. Z.: Wave-induced transport of atmospheric constituents and its effect on the mesospheric Na layer. J. Geophys. Res.-Atmos., 115(D20). https://doi.org/10.1029/2010JD014140, 2010.

Gardner, C. S.: Impact of atmospheric compressibility and Stokes drift on the vertical transport of heat and constituents by gravity waves. J. Geophys. Res.-Atmos., 129(8), e2023JD040436.

365   https://doi.org/10.1029/2023JD040436, 2024.

Gerding, M., Hoffner, J., Lautenbach, J., Rauthe, M., & Lubken, F.: Seasonal variation of temperatures between 1 and 105 km altitude at 54◦ N observed by lidar. Atmos. Chem. Phys., 8(4), 16175-16218. https://doi.org/10.5194/acp-8-7465-2008, 2008.

Guo, Y., & Liu, A. Z.: Seasonal variation of vertical heat and energy fluxes due to dissipating gravity

370   waves in the mesopause region over the Andes. J. Geophys. Res.-Atmos. (3), e2020JD033825. https://doi.org/10.1029/2020JD033825, 2021.

Huang, W., Chu, X., Gardner, C. S., Carrillo-Sánchez, J. D., Feng, W., Plane, J. M., & Nesvorný, D.: Measurements of the vertical fluxes of atomic Fe and Na at the mesopause: Implications for the velocity of cosmic dust entering the atmosphere. Geophys. Res. Lett., 42(1), 169-175.

375   https://doi.org/10.1002/2014GL062390, 2015.

Kawahara, T. D., Gardner, C. S., & Nomura, A.: Observed temperature structure of the atmosphere above Syowa Station, Antarctica (69 S, 39 E). J. Geophys. Res.-Atmos., 109(D12). https://doi.org/10.1029/2003JD003918, 2004.

Li, T., Fang, X., Liu, W., Gu, S.-Y., & Dou, X.: Narrowband sodium lidar for the measurements of

380   mesopause region temperature and wind. Appl. Optics, 51(22), 5401-5411. https://doi.org/10.1364/AO.51.005401, 2012.

Li, T., Ban, C., Fang, X., Li, J., Wu, Z., Feng, W., et al.: Climatology of mesopause region nocturnal temperature, zonal wind and sodium density observed by sodium lidar over Hefei, China (32 N, 117 E). Atmos. Chem. Phys., 18(16), 11683-11695. https://doi.org/10.5194/acp-18-11683-2018, 2018.

385   Li, T., Ban, C., Fang, X., Li, F., Cen, Y., Lai, D., et al.: Seasonal variation in gravity wave momentum

and heat fluxes in the mesopause region observed by sodium lidar. J. Geophys. Res.-Atmos., 127(23), e2022JD037558. https://doi.org/10.1029/2022JD037558, 2022.

Liu, A. Z., & Gardner, C. S.: Vertical dynamical transport of mesospheric constituents by dissipating gravity waves. J. Atmos. Sol.-Terr. Phys., 66(3-4), 267-275.

390 https://doi.org/10.1016/j.jastp.2003.11.002, 2004.

Liu, A. Z., & Gardner, C. S.: Vertical heat and constituent transport in the mesopause region by dissipating gravity waves at Maui, Hawaii (20.7 N), and Starfire Optical Range, New Mexico (35 N). J. Geophys. Res.-Atmos., 110(D9). https://doi.org/10.1029/2004JD004965, 2005.

Mertens, C. J., Mlynczak, M. G., López-Puertas, M., Wintersteiner, P. P., Picard, R., Winick, J. R., et

395 al.: Retrieval of mesospheric and lower thermospheric kinetic temperature from measurements of CO_2 15 μm Earth Limb Emission under non-LTE conditions. Geophys. Res. Lett., 28(7), 1391-1394. https://doi.org/10.1029/2000GL012189, 2001.

Pan, W., & Gardner, C. S.: Seasonal variations of the atmospheric temperature structure at South Pole. J. Geophys. Res.-Atmos., 108(D18). https://doi.org/10.1029/2002JD003217, 2003.

400 She, C., & Yu, J.: Simultaneous three-frequency Na lidar measurements of radial wind and temperature in the mesopause region. Geophys. Res. Lett., 21(17), 1771-1774. https://doi.org/10.1029/94GL01417, 1994.

She, C., Thiel, S. W., & Krueger, D. A.: Observed episodic warming at 86 and 100 km between 1990 and 1997: Effects of Mount Pinatubo eruption. Geophys. Res. Lett., 25(4), 497-500.

405 https://doi.org/10.1029/98GL00178, 1998.

She, C. Y., Yan, Z. A., Gardner, C. S., Krueger, D. A., & Hu, X.: Climatology and seasonal variations of temperatures and gravity wave activities in the mesopause region above Ft. Collins, CO (40.6 N, 105.1 W). J. Geophys. Res.-Atmos., 127(11), e2021JD036291. https://doi.org/10.1029/2021JD036291, 2022.

410 Sheng, Z., He, Y., Wang, S., Chang, S., Leng, H., Wang, J., et al.: Dynamics, chemistry, and modelling studies in the aviation and aerospace transition zones. The Innovation. https://doi.org/10.1016/j.xinn.2025.101012, 2025.

States, R. J., & Gardner, C. S.: Thermal structure of the mesopause region (80–105 km) at 40° N latitude. Part I: Seasonal variations. J. Atmos. Sci., 57(1), 66-77. https://doi.org/10.1175/1520-

415 0469(2000)057<0066:TSOTMR>2.0.CO;2, 2000.

Vincent, R., & Reid, I.: HF Doppler measurements of mesospheric gravity wave momentum fluxes. J. Atmos. Sci., 40(5), 1321-1333. https://doi.org/10.1175/1520-0469(1983)040<1321:HDMOMG>2.0.CO;2, 1983.

Walterscheid, R.: Dynamical cooling induced by dissipating internal gravity waves. Geophys. Res. Lett., 8(12), 1235-1238. https://doi.org/10.1029/GL008i012p01235, 1981.

Weinstock, J.: Heat flux induced by gravity waves. Geophys. Res. Lett., 10(2), 165-167. https://doi.org/10.1029/GL010i002p00165, 1983.

Wu, Q., Ortland, D., Killeen, T., Roble, R., Hagan, M., Liu, H. L., et al.: Global distribution and interannual variations of mesospheric and lower thermospheric neutral wind diurnal tide: 1. Migrating tide. J. Geophys. Res.-Space Phys., 113(A5). https://doi.org/10.1029/2007JA012542, 2008.

Wang, X., Fang, X., Gao, W., Chen, X., Liu, T., Yang, C., Chen, T., Li, T., and Xue, X.: Observation data of a narrow sodium lidar from February 2024 to January 2025. V1. Science Data Bank. https://doi.org/10.57760/sciencedb.27247, 2025.